

# **Influence of powder distribution on process stability in laser beam melting: Analysis of melt pool dynamics by numerical simulations**

F.-J. Gürtler<sup>1,2</sup>, M. Karg<sup>1,2</sup>, M. Dobler<sup>1,2</sup>, S. Kohl<sup>1,2</sup>, I. Tzivilsky<sup>3</sup> and M. Schmidt<sup>1,2</sup>

<sup>1</sup> Institute of Photonic Technologies, Friedrich-Alexander-Universität Erlangen-Nürnberg (FAU),  
Department of Mechanical Engineering, Konrad-Zuse-Str. 3-5, 91052 Erlangen, Germany

<sup>2</sup> Erlangen Graduate School in Advanced Optical Technologies (SAOT), Friedrich-Alexander-  
Universität Erlangen-Nürnberg, Paul-Gordan-Str. 6, 91052 Erlangen, Germany

<sup>3</sup> Kazan National Research Technical University, Department of Laser Technologies,  
K. Marx Str. 10, 420111, Kazan, Russia

REVIEWED

## **Abstract**

The occurrence of defects in the additive manufacturing process of laser beam melting in metal powder bed can be reduced through empiric parameter optimization – but knowledge about basic effects like the influence of the composition of the powder layer on the melt pool is still limited. Particle size distribution and powder layer inhomogeneity after layer coating influence melt pool dynamics and may cause defects in the work pieces. This correlation can hardly be analyzed in experiments, so a three-dimensional transient numerical simulation model is used. The model is based on the continuity equation, the heat equation and the Navier-Stokes equation. Therefore, the finite-volume method capabilities in OpenFOAM are used. The free surfaces of the multi-phase system are calculated using the volume of fluid method. The powder beds have unimodal or bimodal distributions without random effects in the particle composition. Their density and thermal conductivity is adapted to reality. The investigations of the melt pool and the porosity formation demonstrate an advantage of more and smaller particles in the powder for compensation of defects in the powder bed, similar to the results of the experiments.

## **Introduction**

Laser beam melting (LBM), also named selective laser melting (SLM), is an additive manufacturing process, which is one of the most innovative manufacturing technologies. In the LBM technique a laser beam heats and melts lines of a material powder bed. The single molten tracks form a flat structure, which can have filigree as well as massive areas. After a new powder coating the process is repeated and the single layers compose a three-dimensional part.

With this new process many materials like metals, ceramics, etc. can be treated. The workability is influenced by various consolidation mechanisms, as shown by current research [Kruth et al., 2007]. Therefore, the choice of the process parameter is crucial to get high quality products and to minimize residual porosity.

In the current studies of this young manufacturing method the influence of individual process parameters is not yet understood sufficiently [Zheng et al. 2012]. In LBM various dynamical phenomena like wetting, solidification and grain growth are induced as a result of the high temperature gradients [Das, 2003]. To reduce expensive experiments and to enable direct observation of the process dynamics for analysis, numerical models are necessary. There are several simulation methods, which interpret the powder bed as homogeneous bulk material with adapted properties. A finite element method with thermo-mechanical effects was used to

investigate the impact of heat on residual stresses and deformations [Zäh et al., 2009]. A first inhomogeneous powder layer was composed of regions with differing powder densities for a non-uniform behavior of the powder bed in the process [Xiao and Zhang, 2007]. The absorption of the laser energy and thermal conductivity in an irregular powder bed was determined using an analytical model [Gusarov and Smurov, 2010]. A two-dimensional lattice Boltzmann method shows a significant effect of the powder density of the powder bed on the melt pool dynamics [Körner et al., 2011].

All of these simulations do not show the influence of powder beds of various particle sizes and defects in the powder beds on the process. Since pores can arbitrarily appear in the workpiece, our approach is that defects in the powder layer after coating are potential seeds for these pores. However, these defects can occur in reality during layer coating (figure 1). Our second approach is that the impact of these coating defects can be affected by the size distribution of the powder particles. Therefore, our goal is to investigate the influence of inhomogeneities in the powder bed onto the melt pool characteristics and the process stability. Additionally, we want to show the effects of different particle size distributions on this investigation of the process behavior. By these findings, a suitable particle size distribution can reduce the porosity of the work piece and the part quality can be improved at usually too high scan speeds. So the productivity of the LBM process can be increased. Experiments have randomly distributed defects and an analysis of the process and the dynamics of pore development is hardly possible. In contrast, effects of coating defects and different particle size distributions on the process can be analyzed separately and visualized by numerical methods. This simulative analysis is conducted using our three-dimensional numerical simulation model for LBM. Finally, the results are compared to experimental data.

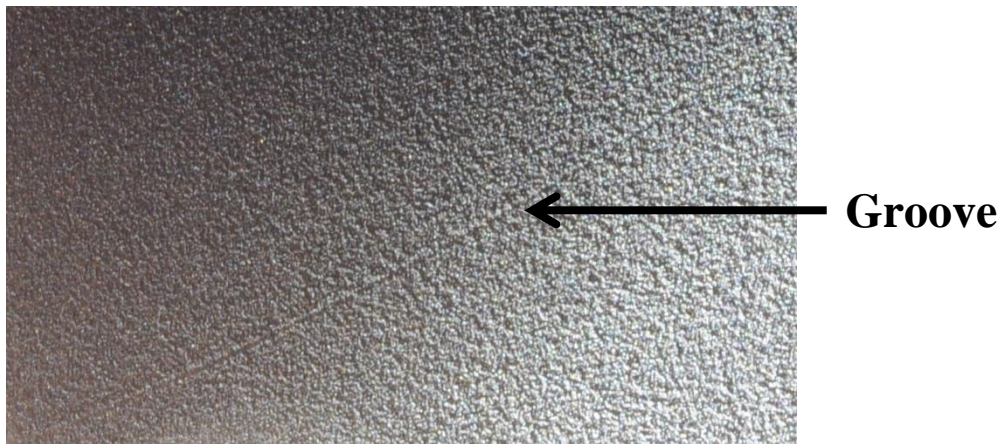


Fig. 1. Groove in the powder bed after layer coating

## Simulation Model

OpenFOAM (Open Field Operation And Manipulation, ©OpenCFD Limited) is a computational fluid dynamics toolbox. The software was developed to address continuum mechanical dynamical problems of heat transfer and multiphase flow using a finite volume formulation on an unstructured grid. The model for solving the specific physical phenomena of laser beam processing was developed at the Institute of Photonic Technologies [Geiger et al., 2009]. This model was adapted for laser beam melting and capabilities for powder representation were implemented [Gürtler et al., 2013]. A combination of multiple physical effects is necessary for this process simulation. The numerical scheme PIMPLE, a combination of PISO and SIMPLE, of OpenFOAM is used for the coupled calculation of the fluid dynamics which is given by the incompressible Navier-Stokes equation

$$\rho \frac{\partial \vec{u}}{\partial t} + \rho \vec{u} \cdot \nabla \vec{u} = -\rho \nabla p + \eta \Delta \vec{u}$$

and the continuity equation for mass conservation

$$\frac{\partial \rho}{\partial t} + \nabla(\rho \vec{u}) = 0$$

The volume of fluid (VOF) method describes the free surface between the molten metal and the ambient atmosphere. The surface dynamics is mainly determined by the evaporation pressure and surface tension.

The phase transitions have the strongest influence on the temperature field. The thermal effects of fusion and evaporation are included in our model. The temperature field is calculated by iteratively solving the heat equation [Kohl et al., 2012]:

$$\frac{\partial}{\partial t}(\rho \cdot H) + \nabla \cdot (\rho \cdot \vec{u} \cdot H) - \nabla \cdot (\lambda \cdot \nabla T) = Q_A$$

The laser beam is modeled as a continuum intensity field perpendicular to the powder bed with Gaussian distribution and focal position at the top of the powder layer.

$$Q_L = \frac{P_L}{2\pi w_0} e^{-\frac{2(x^2+y^2)}{w_0^2}}$$

The absorption on the material surface is calculated and the reflections result in discrete rays. They lead to additionally absorbed energy and end in the material at low ray intensity or after twenty reflections. The reflectance depends on the wavelength, angle of incidence and polarization, as specified by the Fresnel equations

$$R_{\parallel} = \left( \frac{n^2 \cdot \cos(\alpha) - \sqrt{n^2 - \sin^2(\alpha)}}{n^2 \cdot \cos(\alpha) + \sqrt{n^2 - \sin^2(\alpha)}} \right)^2$$

for the parallel polarized part of the laser beam and

$$R_{\perp} = \left( \frac{(\cos(\alpha) - \sqrt{n^2 - \sin^2(\alpha)})^2}{n^2 - 1} \right)^2$$

for the vertical polarized part.

The transmission of the laser beam follows the Beer-Lambert law

$$Q_T = (Q_L - Q_R) \cdot e^{-\kappa \cdot l}$$

The physical properties and process parameters are listed in Table 1 and Table 2.

Table 1: Physical properties [Nogowizin, 2003]

Physical property of AlSi10Mg	Symbol	Unit	Value
Density	$\rho$	kg/m <sup>3</sup>	2382
Specific heat	$cp$	J/(kg·K)	1027
Thermal conductivity	$k$	W/(m·kg)	175
Kinematic viscosity of liquid	$\nu$	m <sup>2</sup> /s	1·10 <sup>-6</sup>
Solidus temperature	$T_M$	K	830
Liquidus temperature	$T_S$	K	869
Vaporization temperature	$T_V$	K	2700
Enthalpy of fusion	$H_M$	J/kg	417·10 <sup>3</sup>
Enthalpy of vaporization	$H_V$	J/kg	12·10 <sup>6</sup>
Surface tension coefficient	$\sigma$	N/m	0.9
Complex refractive index ( $\lambda = 1.064 \mu\text{m}$ )	$n+k \cdot i$	-	1.37 + 9.49·i

Table 2: Process parameters

Process parameter	Symbol	Unit	Value
Laser power	$P_L$	W	100
Focus radius	$w_0$	$\mu\text{m}$	10
Feed velocity	$v_0$	m/s	0.75
Wavelength	$\lambda$	nm	1064
Scan spacing	$s$	$\mu\text{m}$	50

## Properties of the Particle Size Distributions and Powder Beds

For the analysis of the process stability against voids in the powder bed, we investigate different powder size distributions in LBM by simulations and experiments. The material of the powder particles is AlSi12Mg (EN AC 43000) and it is produced under argon atmosphere by TLS Technik GmbH & Co. Spezialpulver KG.

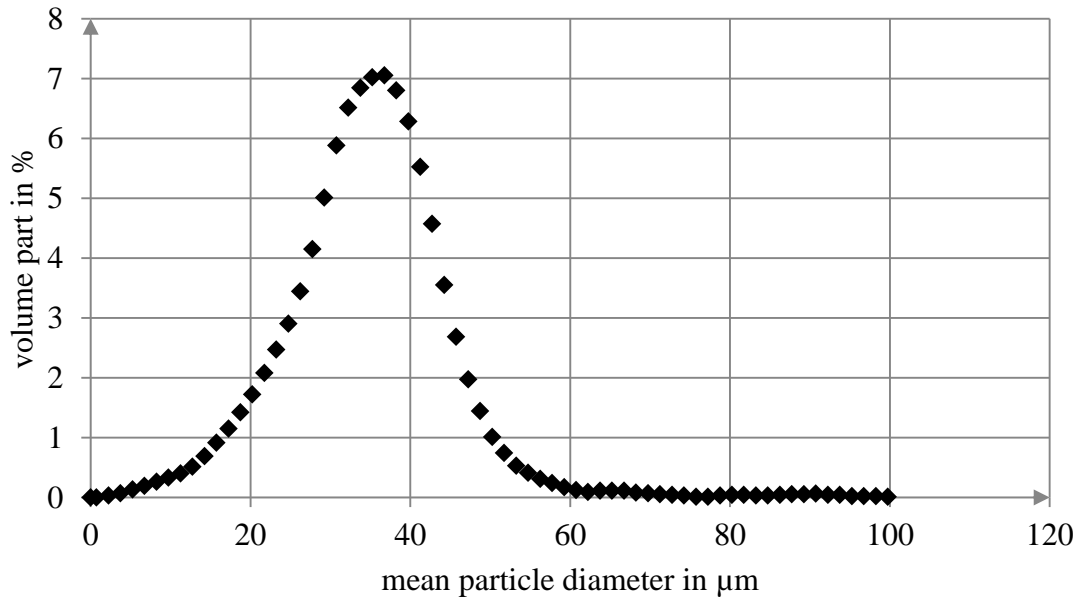


Fig. 2. The particle size distribution of AlSi10Mg produced under argon atmosphere: The measurement precision is 1.5  $\mu\text{m}$ .

The particle size distribution is measured with the dynamic image analysis method according to standard ISO 13322-2, see figure 2. This original powder is filtered in various size ranges. These fractions are mixed together by different volume fractions (table 3). The new mixtures of powder particles are investigated in the following by simulations and experiments.

Table 3: Powder combinations of different particle sizes and volume fractions

Powder name	Size range of fraction 1 in $\mu\text{m}$	Size range of fraction 2 in $\mu\text{m}$	Ratio of mass fractions
Al_20+32-40	0-20	32-40	10 % : 90 %
Al_20+40-50	0-20	40-50	10 % : 90 %
Al_20+50-63	0-20	50-63	10 % : 90 %
Al_20+40_3-7	20-32	40-50	30 % : 70 %
Al_20+40_4-6	20-32	40-50	40 % : 60 %
Al_20+40_5-5	20-32	40-50	50 % : 50 %

In our simulations the powder particles are represented by spheres. This assumption is valid because the shape of particles produced under argon atmosphere is almost spherically (figure 3).

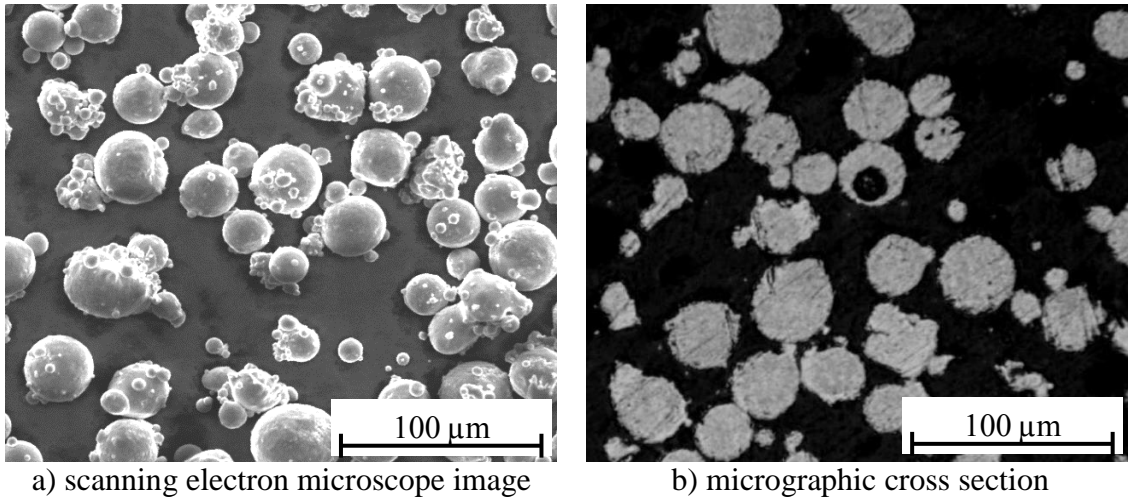


Fig. 3. Illustration of the powder particles: a) SEM image, b) micrographic cross section

In our simulations, the size distribution between the upper and lower limit of a fraction is averaged to one particle size  $\bar{d}_k$  using the distribution of the particle sizes as averaging weight (figure 2):

$$\bar{d}_k = \frac{\sum p_l \cdot d_l}{\sum p_l}$$

with the particle size  $d_l$  of each measurement point  $l$ , the normalized number of particles  $p_l = \frac{d_{3,l}}{m_l}$  and the mass of the particle  $m_l = \rho \cdot \frac{3}{4} \pi \left(\frac{d_l}{2}\right)^3$ .

This enables the representation of bimodal powder mixtures in the different blends. Using the mean powder size and the volume fractions we calculate the ratio  $r_i$  of the single particles for each powder mixture  $i$ , which is given by the normalized particle quantities of each powder part in table 4.

$$r_i = \frac{\frac{f_{i,1}}{V_{i,1}}}{\frac{f_{i,2}}{V_{i,2}}}$$

with the ratio of mass fractions  $f_{i,1}$  and  $f_{i,2}$  and the single particle volume of each particle fraction  $V_{i,j} = \frac{3}{4} \pi \left(\frac{\bar{d}_k}{2}\right)^3$  (with mean size  $\bar{d}_k$ ).

Table 4: Discrete particle size distributions

Powder name	Mean size of fraction 1 in $\mu\text{m}$	Mean size of fraction 2 in $\mu\text{m}$	Ratio of particles
Al_20+32-40	14.8	35.5	1.5 : 1
Al_20+40-50	14.8	43.5	2.8 : 1
Al_20+50-63	14.8	53.0	5.1 : 1
Al_20+40_3-7	25.5	43.5	2.1 : 1
Al_20+40_4-6	25.5	43.5	3.3 : 1
Al_20+40_5-5	25.5	43.5	5.0 : 1

The powder particles under  $10 \mu\text{m}$  agglomerate and can be regarded as components of large particles (figure 3a). Also they cannot be displayed as individual particles in the simulation volume except we drastically increase the spatial discretization. So the distribution size between 0 and  $20 \mu\text{m}$  is reduced to 10 to  $20 \mu\text{m}$  in the simulations.

Table 5: Discrete particle size distributions adapted to simple ratios

Powder name	Mean size of fraction 1 in $\mu\text{m}$	Mean size of fraction 2 in $\mu\text{m}$	Ratio of particles
Al_20+32-40	14.7	35.0	3 : 2
Al_20+40-50	14.7	44.0	3 : 1
Al_20+50-63	14.7	55.6	6 : 1
Al_20+40_3-7	24.4	44.0	5 : 2
Al_20+40_4-6	24.2	44.0	4 : 1
Al_20+40_5-5	24.2	44.0	6 : 1

A regular arrangement of the powder particles is chosen to exclude random effects of the powder bed in the simulations and to have a plain test case. Therefore, we define unit cells of particles, which can easily be arranged for a powder layer or cluster. These unit cells have to include the correct particle quantities of both fractions. Since we want to use only whole particles, the particle quantities of both fractions in the unit cells need to be integers. Thus, we have to slightly round the particle sizes of the fractions to reach small unit cells. In our simulation of single layers the unit cells have to be smaller than the height of the loose powder layer. The particle sizes and quantities of the different fractions in the unit cells that can be found in table 5 are used in the simulations.

Furthermore the powder densities and the thermal conductivities of the powder beds have to be considered. The equation for the powder density is given as

$$\rho_i = \frac{q_{i,1} \cdot V_{i,1} + q_{i,2} \cdot V_{i,2}}{V_{i,cell}}$$

with the volume of the unit cell  $V_{cell} = f_{cell} \cdot h_{cell}$  (with height of simulated powder layer  $h_i$ ), the single particle volume of each particle fraction  $V_{i,j} = \frac{3}{4}\pi \left(\frac{\bar{d}_k}{2}\right)^3$  (with mean size  $\bar{d}_k$ ) and the quantity of each particle size  $q_{i,j}$  in the unit cell.

The kind of arrangement of the powder particles is specified clearly. The powder density, however, can be modified by introducing and varying minimum distances between the spheres. Additionally, the distances reduce the interfaces between the particle spheres to decrease the thermal conductivity. Because of these two reasons, a distance of 2  $\mu\text{m}$  is chosen to obtain the results shown in table 6 and 7. The resulting powder bed of the different particle size mixtures can be taken from figure 4.

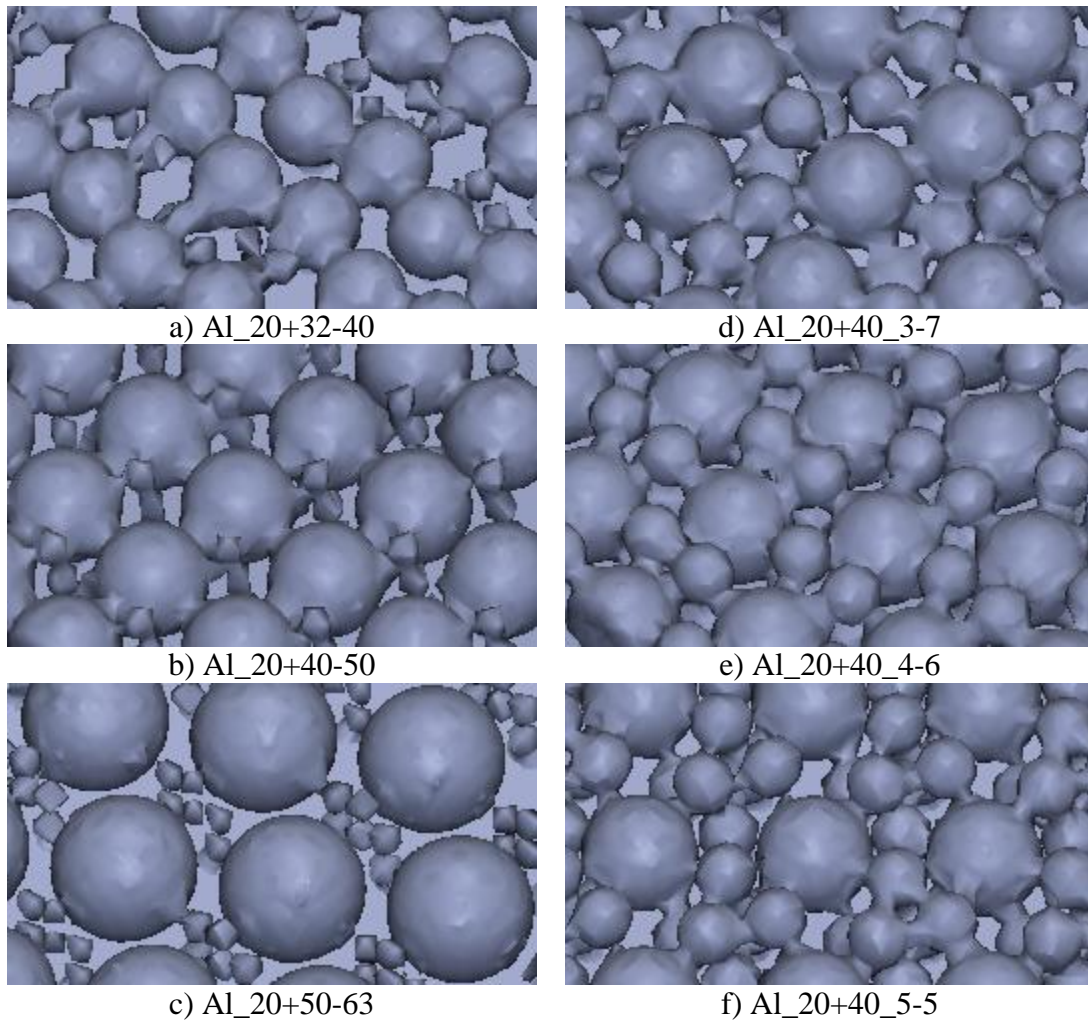


Fig. 4. Illustration of the different powder beds (a-f): The connections between the single particles are caused by the displaying method: If there is no completely empty mesh cell (without metal) in between two particle spheres, the displaying algorithm cannot calculate a surface that separates the two particles

Table 6: Height and density of one powder layer in the simulations

Powder name	Powder density of layer in sim.	Height of sim. powder in $\mu\text{m}$	Thickness of sim. layer in $\mu\text{m}$
Al_20+32-40	0.47	37.0	17.4
Al_20+40-50	0.49	46.0	22.5
Al_20+50-63	0.45	57.6	25.9
Al_20+40_3-7	0.48	46.0	22.1
Al_20+40_4-6	0.49	52.4	25.7
Al_20+40_5-5	0.47	46.0	21.6

An investigation of the resulting powder layers delivers the results in table 6. The powder density of the powder layer varies between 45 % and 49 %. The height of the simulated powder layer mainly depends on the largest particles and ranges from 37  $\mu\text{m}$  to 57.6  $\mu\text{m}$ . The calculated resulting layer thickness of the simulated powder bed after complete melting is between 17.4  $\mu\text{m}$  and 25.9  $\mu\text{m}$ , which is comparable to the 30  $\mu\text{m}$  layer in our experiments.

Table 7: Powder density and thermal conductivity of loose powder in experiments and simulations

Powder name	Powder density in experiments	Powder density in simulations	Ratio of therm. cond. in sim.
Al_20+32-40	0.56	0.53	0.42
Al_20+40-50	0.58	0.51	0.23
Al_20+50-63	0.55	0.45	0.13
Al_20+40_3-7	0.53	0.51	0.28
Al_20+40_4-6	0.54	0.51	0.29
Al_20+40_5-5	0.55	0.52	0.26

For an experimental comparison we investigate loose powder (column 2 in table 7). The powder density of the real powder is measured according to standard DIN EN ISO 3923-1:2010-08 for loose powder. The values vary between 53 % and 58 %. These values cannot be compared to the powder density of the layers in the simulation directly (table 6), since the geometric boundary conditions differ. Thus, we have to determine the powder densities of simulated loose powder, which range from 45 % to 53 % (column 3 in table 7). Most powder mixtures agree with the real powders or are slightly undervalued. Additionally to this, the powder density of the powder layer in the simulation is less. Both facts agree to the approach that the powder density of metal powder is reducing at the layer coating by a wiper.

Furthermore, the ratio of the thermal conductivity of the loose simulated powder to a solid body out of the same material ascertained in the plane of the layer, which is the plane crucial for the process, is given as

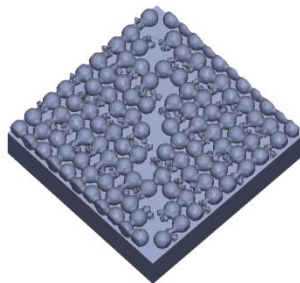
$$r_{\lambda} = \frac{\lambda_{\text{powder}}}{\lambda_{\text{bulk}}}$$

The ratio is between 13 % and 42 % (column 4 in table 7). A look to the ratio of the thermal conductivities between powder and solid body in the simulation near room temperature shows too high values since the thermal conductivity of powder should be around ten times of the atmosphere gas, arising  $\sim 0.2 \text{ W}/(\text{m}\cdot\text{K})$  for argon [Rombouts et al., 2005]. If we increase the distance between the spheres, the thermal conductivity would be reduced, but also the powder density. For example, a distance of  $5 \mu\text{m}$  in the powder bed Al\_20+40\_4-6 leads to a ratio of thermal conductivities of 6 %, however also to a powder density of around 40%, which is much smaller than the density of 54 % in the real loose powder. Thus, the thermal conductivity in our simulation does not reach the values in the literature [Zeng et al., 2012]. As one reason we assume the numerical discretization between the particles, which result in overestimated particle connections. Additionally, other aspects like oxide layers, which cannot yet be displayed in our simulation model, can lead to a reduced thermal conductivity in the powder material.

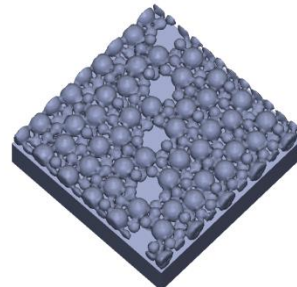
The properties of the powder bed in the process chamber of the LBM machines can hardly be determined experimentally. On the one hand the verification methods like camera imaging have not the resolution to resolve single particles. On the other hand methods like scanning electron microscope or laser scanning microscope cannot be set up in the process chamber. Regarding the currently available verification methods for the powder bed in commercial machines like the measurement of the powder density, we state a good agreement of the real and the modeled properties of the powder beds. The powder density of the powder mixtures, which is the most important property, accords with the real loose powder and the powder layer is satisfactorily represented. Unfortunately, the thermal conductivity of the powder layer is too high at room temperature. But it highly increases with the temperature [Zehner, 1972], especially by effects of sintering. Besides, the capillary actions between the particles and the melt [Gürtler et al., 2013] drastically change the properties of the powder bed and consequently the thermal conductivity at the main focus of the process. Thus, the additional distance between the particles can be considered as correctly chosen.

## Process Setup

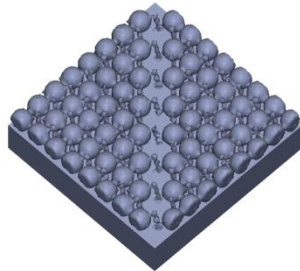
For the investigation of the influence of different powder beds on the process a workspace of  $400 \times 400 \times 200 \mu\text{m}$  is analyzed. The temperature in this box is set to 500 K at the start time. The material and energy can flow through the boundaries, except for the bottom side. The temperature under an  $80 \mu\text{m}$  thick metal plate is set to constantly 500 K, since that allows displaying the high energy loss by the already molten and solidified layers. The length of each line processed with the laser beam in the powder bed is  $300 \mu\text{m}$  long. The first line is  $50 \mu\text{m}$  beside the middle of the workspace, the second is in the middle and the last line is located  $50 \mu\text{m}$  further. As in the experiments, the line spacing is  $50 \mu\text{m}$ , the feed rate is  $0.75 \text{ m/s}$ , the laser power is  $100 \text{ W}$ , the wavelength is  $1064 \text{ nm}$  and the beam waist is  $10 \mu\text{m}$  (table 2). The simulations are done for the presented regular powder beds and for imperfect powder beds, in which the large particles along the diagonal of the workspace are missing, see figure 5. Thus we can investigate the influence of defects in the powder bed on the process.



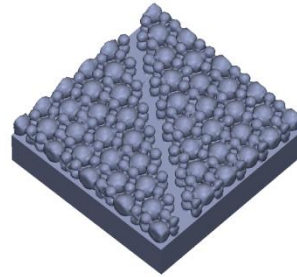
a) Al<sub>20</sub>+32-40



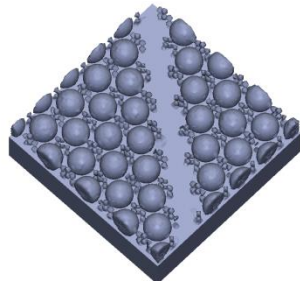
d) Al<sub>20</sub>+40\_3-7



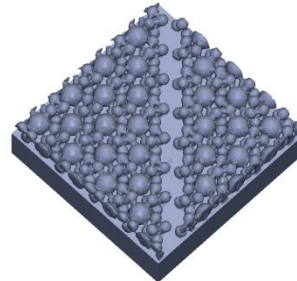
b) Al<sub>20</sub>+40-50



e) Al<sub>20</sub>+40\_4-6



c) Al<sub>20</sub>+50-63



f) Al<sub>20</sub>+40\_5-5

Fig. 5. Illustration of the different powder beds with missing large particles along the diagonal of the workspace (a-f)

## Results and Discussion

### Experimental results

For comparison experiments are carried out with the same parameters as in the simulations and a layer thickness of 30  $\mu\text{m}$ . Cubes with 5 mm edge length are built on the machine SLM 50 by ReaLizer GmbH and their relative densities are investigated, see figure 6. The values of these results are split in three different groups. For later comparison to the simulation we define a green quality class for values over 98 %, yellow for 97-98 % and red for values lower than 97 % relative density. Accordingly, the green group represents more dense work pieces than the orange ones and red for worse subjects. It is identifiable that powder blends with more and smaller particle lead to a higher relative density in the test samples. Consequently, the powder bed after layer coating has better properties for the production of homogenous layers.

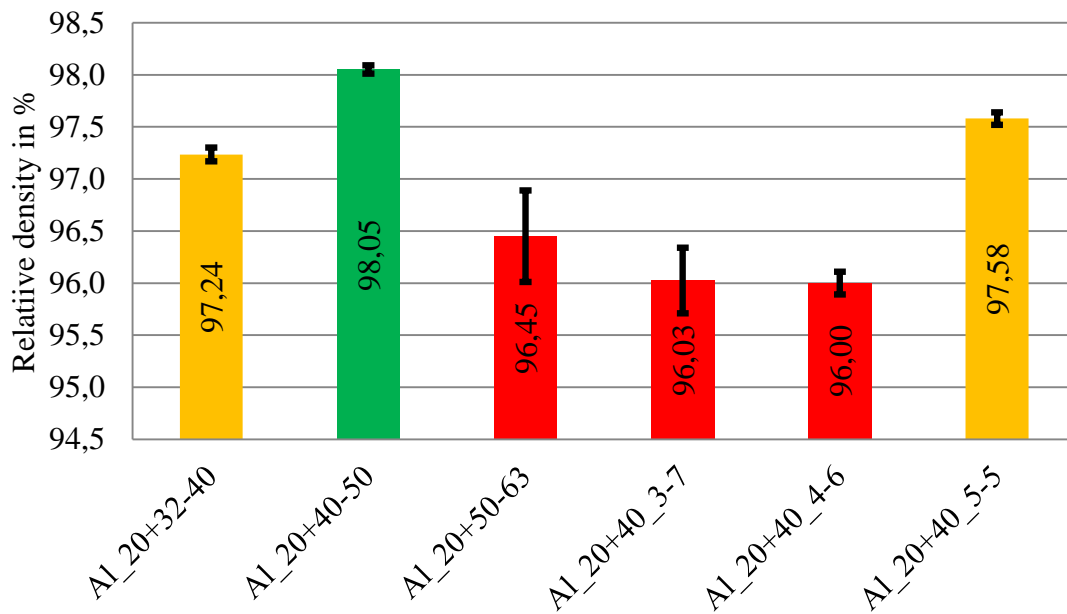
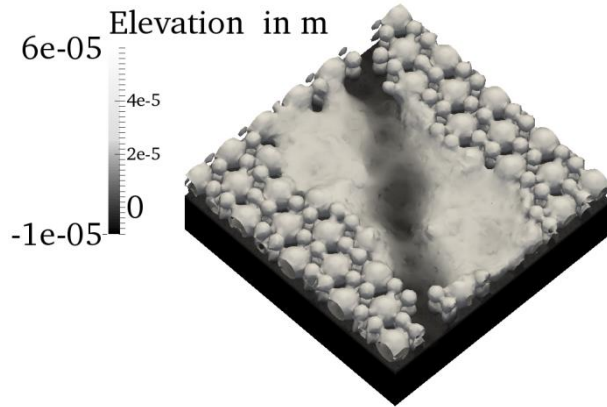
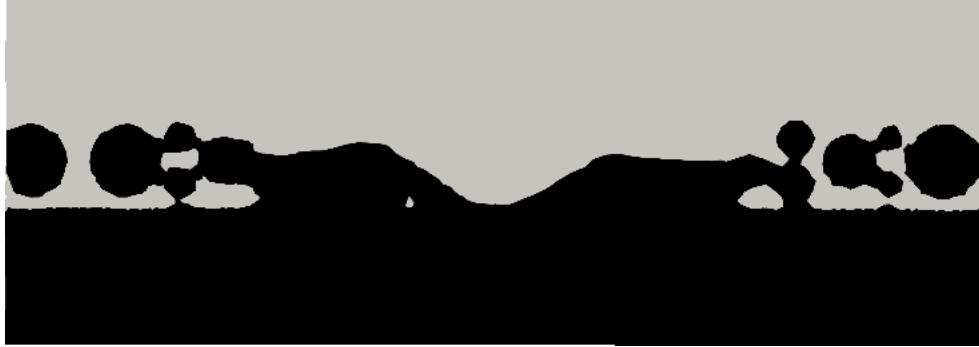


Fig. 6. Relative densities of the experimental structures: They are divided in three quality classes (green: > 98 %; orange: 97-98 %; red: < 97 %).

### Analysis of the simulated layer thickness



a) Top view of the powder bed (Elevation of 0  $\mu\text{m}$  at top of the metal plate)



b) Cross-section orthogonal to the line of the missing particles

Fig. 7. Illustration of three molten scan lines for the powder beds Al\_20+40\_4-6 with missing large particles along the diagonal of the workspace

In the next step we investigate the thickness of the resulting layers. An outcome can be taken from figure 7a where the three molten tracks of the inhomogeneous powder beds Al\_20+40-50 and Al\_20+40\_4-6 are shown. A groove is formed along the missing spheres, which is distinctively visible in figure 7b. In the following we analyze this by various measurements, starting with a theoretical analysis.

Table 8: Theoretical layer thickness for regular and inhomogeneous powder beds calculated using the powder density and the relative height of the layer at defects

Powder name	Theoretical height in $\mu\text{m}$	Height at missing spheres in $\mu\text{m}$	Relative height
Al_20+32-40	17.2	9.5	0.55
Al_20+40-50	23.4	2.4	0.10
Al_20+50-63	26.1	2.6	0.10
Al_20+40_3-7	21.9	14.2	0.65
Al_20+40_4-6	25.6	10.2	0.40
Al_20+40_5-5	21.7	10.8	0.50

Using the powder height and powder density (from table 6), we calculate the theoretical thickness of the powder layers in the unit cells of the particles. In the second column of table 8 the theoretical heights  $h_{i,theo,reg}$  of the regular layer are shown for the different powder beds. In the next column the theoretical heights  $h_{i,theo,imp}$  of the powder beds, in which the large particles at the diagonal are missing, are determined in the calculations by removing the volume of the missing sphere in the unit cells. In the last column the relative height  $r_{i,theo}$ , which is the ratio between the inhomogeneous and regular powder bed, is calculated to give a better comparison:

$$r_{i,theo} = \frac{h_{i,theo,imp}}{h_{i,theo,reg}} = \frac{\frac{q_{i,1} \cdot V_{i,1} + (q_{i,2} - 1) \cdot V_{i,2}}{A_{i,cell}}}{\frac{q_{i,1} \cdot V_{i,1} + q_{i,2} \cdot V_{i,2}}{A_{i,cell}}}$$

with the area  $A_{i,cell}$  at the bottom of the unit cell and previously defined variables  $q_{i,j}$  and  $V_{i,j}$ .

Table 9: Simulated layer thickness after solidification in the middle of the workspace for the regular and inhomogeneous powder beds and the relative height of the layer at defects

Powder name	Simulated height in $\mu\text{m}$	Height at missing spheres in $\mu\text{m}$	Relative height
Al_20+32-40	12	4	0.33
Al_20+40-50	24	2	0.08
Al_20+50-63	26	0	0.00
Al_20+40_3-7	22	0	0.00
Al_20+40_4-6	22	0	0.00
Al_20+40_5-5	18	5	0.28

The same analysis is carried out for the heights  $h_{i,sim,reg}$  and  $h_{i,sim,imp}$  within the simulations (table 9). We measure the layer thickness in the middle unit cell of the workspace, which means in the middle of the second scan line. The measured minimum height inside the unit cell of the particles is used as the layer thickness to avoid influences of the geometry of the particle arrangement. The simulated layer heights are similar or smaller than those calculated theoretically. The heights in the simulations with missing spheres vary between 0 and 5  $\mu\text{m}$ . This means that the relative heights  $r_{i,sim}$ , which are defined as the ratio between the simulated heights of the regular powder beds to those of the inhomogeneous powder beds at the position of the imperfection, reach 28 % maximum:

$$r_{i,sim} = \frac{h_{i,sim,imp}}{h_{i,sim,reg}}$$

Both height measurements for powders with large particles are zero. As a first explanation for this phenomenon we infer that powder beds with small particles can compensate defects in the powder bed better than powder beds with large particles.

For the following analysis we calculate the ratio  $r_{i,imp}$  of the simulated to the theoretical layer heights of the inhomogeneous powder beds (column 3 in table 8 and 9):

$$r_{i,imp} = \frac{h_{i,sim,imp}}{h_{i,theo,imp}}$$

The values are between 0 and 85 %, depicted by bright colors in figure 8. This measurement shows the compensation of defects in the unit cells by melt pool dynamics. As in the experiments (compare figure 6), we can see three quality groups, the red quality class at zero, the bright orange group at around half the value of the green class, which is at 85 %. Thereby we can easily distinguish the powder mixtures for the suitability in LBM. The green group stands for a better compensation of defects in the powder bed and consequently for a better resulting work piece than the orange one and red means a worse quality.

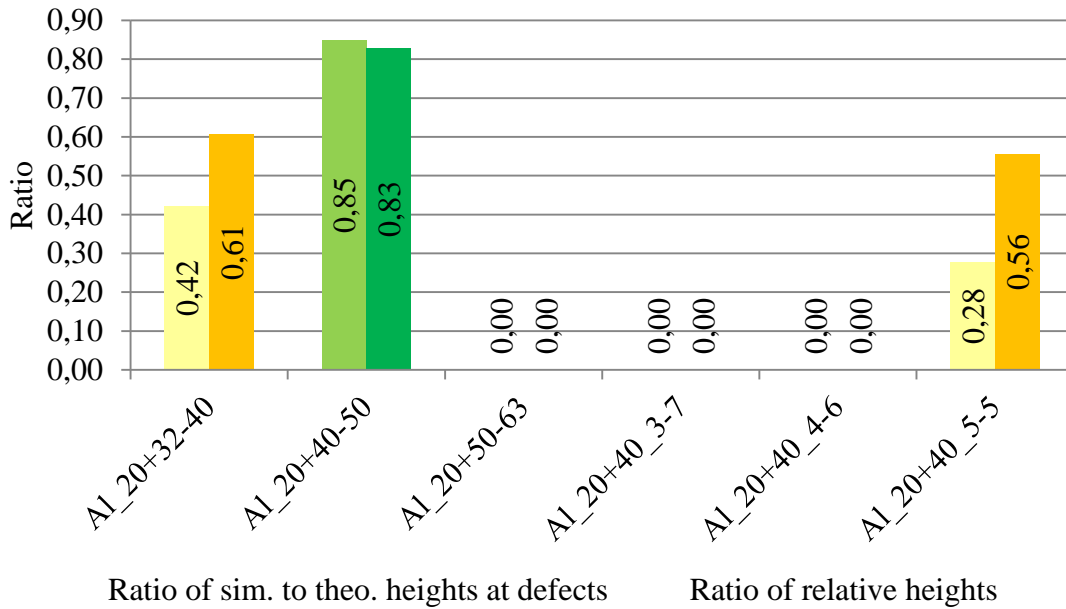


Fig. 8. Ratio of layer heights between simulation and theory at missing spheres in the powder bed (bright colors) and ratio of relative heights between simulation and theory (dark colors): They are split in three quality classes (green: >75 %; orange: 25-75 %; red: <25 %), similar to the experimental results (The red values are zero.).

If we compare the relative layer heights of the simulations to those of the theoretical analysis, we obtain similar results. Therefore, the ratio  $r_i$  of the simulated relative height to the theoretical one is calculated (column 4 in table 8 and 9):

$$r_i = \frac{r_{i,sim}}{r_{i,theo}} = \frac{\frac{h_{i,sim,imp}}{h_{i,sim,reg}}}{\frac{h_{i,theo,imp}}{h_{i,theo,reg}}}$$

Subsequently we get a completely normalized criterion to evaluate the quality of the powder mixtures for LBM. The results are displayed by dark colors in figure 8. We split them in three quality classes with similar values as for the ratio of layer heights. The green group signifies a better conformance of the theoretical defects compensation and again a better process result than the orange one and red agrees worse.

For both ratios the powder mixtures are separated into the same quality classes. The powder Al\_20+50-63, Al\_20+40\_3-7 and Al\_20+40\_4-6 have got the worst results and are in the red class. The mixtures Al\_20+32-40 and Al\_20+40\_5-5 have got ratios of around 0.5 and are in the orange class. The green quality class consists of the powder mixture Al\_20+40-50 and achieves a value of over 80 %. This quality order agrees completely with the findings of the experiments, see figure 6.

Through our simulative fluid-dynamic analysis we can confirm the assumption that powder beds with more and smaller particles compensate defects in the powder bed better by means of melt pool dynamics. Thus, the surface is smoother and the following layer has a more even thickness. As a consequence, the process is producing more actually and there are fewer defects in the work piece, which is confirmed by the experiments.

### Analysis of the simulated melt pool

In this section the melt pool shape is analysed for a deeper process understanding. Its volume is measured at the time when the laser is located in the middle of the second track.

Table 10: Melt pool volume in the middle of the process for regular powder beds and powder beds with defects and their relative volume

Powder name	Volume at reg. beds in $\mu\text{m}^3$	Volume at defects in $\mu\text{m}^3$	Relative volume
Al_20+32-40	$30.4 \cdot 10^3$	$11.8 \cdot 10^3$	0.39
Al_20+40-50	$33.2 \cdot 10^3$	$7.0 \cdot 10^3$	0.21
Al_20+50-63	$73.5 \cdot 10^3$	$37.2 \cdot 10^3$	0.51
Al_20+40_3-7	$34.8 \cdot 10^3$	$9.6 \cdot 10^3$	0.28
Al_20+40_4-6	$42.0 \cdot 10^3$	$18.0 \cdot 10^3$	0.48
Al_20+40_5-5	$56.7 \cdot 10^3$	$30.4 \cdot 10^3$	0.54

The melt pool volume is reduced by defects in the powder layer to a ratio of 21-54 % (table 10). The decrease occurs since the laser beam energy is directly conducted by the solid layers (metal plate) at the bottom because of the missing heat accumulation of the complete

powder layer. However, the outcomes show no clear trends to discriminate the powder beds for process stability.

Table 11: Melt pool depth in the middle of the laser spot in the middle of the process for regular powder beds and powder beds with defects and their relative depth

Powder name	Depth of reg. beds in $\mu\text{m}$	Depth at defects in $\mu\text{m}$	Relative depth
Al_20+32-40	23.5	12.0	0.51
Al_20+40-50	22.4	13.3	0.59
Al_20+50-63	18.0	7.2	0.40
Al_20+40_3-7	21.6	13.3	0.62
Al_20+40_4-6	29.7	22.8	0.79
Al_20+40_5-5	27.9	23.3	0.84

Because in LBM there are no effects similar to the keyhole at laser beam welding, especially at these process parameters, the melt pool depths can be measured in the middle of the laser spot when the laser beam is in the middle of the second line (table 11). The ratios of the melt pool depths of the inhomogeneous to the regular powder beds vary within a range of 40-84 %. These results show a tendency to better preservation of the melt pool depth against defects by more and smaller particles. Hence, this outcome agrees with the evidence of the consolidated layer heights shown in the section before.

## **Summary and Outlook**

A numerical method at the powder scale is used in this paper to investigate the LBM process. We investigate the influence of various particle size mixtures of the material AlSi10Mg and defects in the powder bed onto the melt pool and the porosity formation.

Therefore, we verify the powder representation of our simulation model and ensure that the used powder configurations agree with reality. Despite the thermal conductivities of our powders at room temperature are overestimated due to geometrical constraints, we point out that their thermal conductivity at much higher process temperatures can safely be assumed to match the experimental values more closely. The powder densities of our powders agree well with the experimental values.

First we examine the resulting layer thickness. The measured heights in the simulations normalized to the theoretical calculated heights of the compacted powder layer show a good correlation to the particle size distributions. Furthermore, we investigate the melt pool volume and height. We determine that the powder mixtures with more and smaller particles compensate defects in powder beds better. This leads to a more stable LBM process, which is in accordance with the results of our experimental investigations. In sum, the findings of the current study clearly demonstrate the importance of error free layer coating for porosity formation and overall quality of the LBM process.

Further research will focus on the propagation of defects through several layers. This will enable us to analyze the resulting powder bed whether a compensation of defects is possible.

## **Acknowledgments**

The authors gratefully acknowledge funding of the Erlangen Graduate School in Advanced Optical Technologies (SAOT) by the German Research Foundation (DFG) in the framework of the German excellence initiative and funding of the German Federal Ministry of Education and Research by the funding program Collaborative Research Center SFB814 (Additive Manufacturing), project A5. Work is performed with support of the Ministry of Education and Science of the Russian Federation, the state contract No. 14.Z50.31.0023.

## References

- Das, S., 2003. Physical aspects of process control in selective laser sintering of metals. *Adv. Eng. Mater.* 5, p. 701–711.
- Geiger, M., Leitz, K.-H., Koch, H., Otto, A., 2009. A 3D transient model of keyhole and melt pool dynamics in laser beam welding applied to the joining of zinc coated sheets. *Production Engineering* 3 [2], p. 127-136.
- Gürtler, F.-J., Karg, M., Leitz, K.-H., Schmidt, M., 2013. Simulation of laser beam melting of steel powders using the three-dimensional volume of fluid method. *Phys. Proced.* 41, p. 874–879.
- Gusarov, A. V., I. Smurov, I., 2010. Modeling the interaction of laser radiation with powder bed at selective laser melting. *Physics Procedia* 5, p. 381-394.
- Körner, C., Attar, E., Heinl, P., 2011. Mesoscopic simulation of selective beam melting processes. *J. Mater. Process. Technol.* 211, p. 978–987.
- Kruth, J.-P., Levy, G., Klocke, F., Childs, T.H.C., 2007. Consolidation phenomena in laser and powder-bed based layered manufacturing. *CIRP Ann. – Manufact. Technol.* 56, p. 730.
- Nogowizin, B., 2003. Druckgusslegierungen und ihre Eigenschaften. *Druckguss-Praxis* 4, p. 161-168.
- Rombouts, M., Froyen, L., Gusarov, A.V., Bentefour, E. H., Glorieux, C., 2005. Photopyroelectric measurement of thermal conductivity of metallic powders. *Journal of applied physics* 97, p. 024905.
- Xiao, B., Zhang, Y., 2007. Laser sintering of metal powders on top of sintered layers under multiple-line laser scanning. *J. Phys. D: Appl. Phys.* 40, p. 6725–6735.
- Zäh, M. F., Branner, G., Krol, T.A., 2009. A three dimensional FE-model for the investigation of transient physical effects in Selective Laser Melting. *Innovative Developments in Design and Manufacturing – Adv. Res. in Vir. and Rap. Pro.*
- Zehner, Peter, 1972. Experimentelle und theoretische Bestimmung der effektiven Wärmeleitfähigkeit durchströmter Kugelschüttungen bei mässigen und hohen Temperaturen. Universität Karlsruhe, PhD thesis.
- Zeng, K., Pal, D., Stucker, B., 2012. A review of thermal analysis methods in Laser Sintering and Selective Laser Melting. *Solid Freeform Fabrication Symposium*, vol. 23.